Confidential: not for distribution. Submitted to IOP Publishing for peer review 17 October 2012

DC-Dynamic Biasing for $> 50\times$ Switching Time Improvement in Severely Underdamped Fringing-Field Electrostatic MEMS Actuators

J Small[1], A Fruehling[2], A Garg[2], X Liu[1] and D Peroulis[2]

[1] School of Electrical and Computer Engineering, University of California Davis, Davis, CA 95616 United States of America

[2] Birck Nanotechnology Center and the School of Electrical and Computer Engineering, Purdue University, West Lafayette, IN 47906 United States of America

E-mail: jasmall@ucdavis.edu

Abstract. This paper presents the design and experimental validation of DC-dynamic biasing for $> 50\times$ switching time improvement in severely underdamped fringing-field electrostatic MEMS actuators. The electrostatic fringing-field actuator is used to demonstrate the concept due to its robust device design and inherently low damping conditions. In order to accurately quantify the gap height versus voltage characteristics a heuristic model is developed. The difference between the heuristic model and numerical simulation is less than 5.6% for typical MEMS geometries. MEMS fixed-fixed beams are fabricated and measured for experimental validation. Good agreement is observed between the calculated and measured results. For a given voltage, the measured and calculated displacements are typically within 10%. Lastly, the derived model is used to design a DC-dynamic bias waveform to improve the switching time of the underdamped MEMS actuators. With dynamic biasing, the measured up-to-down and down-to-up switching time of the actuator is ~ 35 μs. On the other hand, coventional step biasing results in a switching time of ~ 2 ms for both up-to-down and down-to-up states.

1. Introduction

Electrostatic actuation for microelectromechanical systems (MEMS) is the most prevalent technique due to its virtually zero power consumption, high energy densities, relatively short switching times, large forces, small device footprints, simplicity in fabrication and testing, and ease of integration with post-CMOS processing. In particular, typical switching times for electrostatic MEMS are on the order of 10s to 100s of microseconds [1] and [2]. This is made possible through careful electromechanical design around the well-known pull-in instability. In these designs, it is standard practice to design the beam to be critically damped as a compromise between up-to-down and down-to-up switching time. The fixed-fixed beam will typically have an underlying electrode that it will pull-down and adhere to, electrostatically, with minimum contact bouncing. Upon release of the applied bias, squeeze film damping between the membrane and the underlying substrate is the physical mechanism that prevents severe ringing and brings the beam quickly to its initial gap height. Several applications that require fast switching and low power consumption (electrostatic actuation) have benefited from MEMS deployed in this manner [3] - [8]. However designs that make contact are susceptibility to dielectric charging and stiction, thereby reducing the robustness of this approach.

Electrostatic fringing-field actuated (EFFA) MEMS is an attractive alternative as a robust actuator. EFFA MEMS have been analyzed and successfully deployed in sensor and actuator applications [9] - [19]. These MEMS are appropriately called "fringing-field" actuated due to the absence of a parallel counter electrode directly beneath the movable membrane (Fig. 1). In the EFFA configuration, the pull-down electrode can be considered as a single electrode that is split into two separate electrodes. These electrodes are laterally offset such that no overlap exists between the moving membrane and the pull-down electrode. This geometry results in effectively zero electrostatic parallel-plate force, permitting EFFA MEMS to benefit from an inherent lack of "pull-in" and continuous and stable displacement throughout the entire vertical gap height [9]. EFFA MEMS have been fabricated with and without the underlying substrate [9] and [19]. In order to demonstrate an extremely underdamped fixed-fixed beam, in this work, the underlying substrate is removed. Consequently, the removal of the substrate from beneath the fixed-fixed beam results in virtually zero squeeze film damping. Which also results in a MEMS device that suffers from severe ringing and long settling times in response to a conventional unit step DC bias. DC-dynamic biasing can potentially reduce the long settling time.

This paper reports on employing DC-dynamic biasing waveforms to significantly improve the switching time of very underdamped and robust electrostatic MEMS actuators [20] - [25]. The waveform concept is derived by exploiting the physical phenomena of the step response of underdamped second order systems. As a result, a $> 50\times$ improvement in switching time is experimentally demonstrated. This paper is outlined as follows. In Section 2 a phenomenological model is developed to quantify

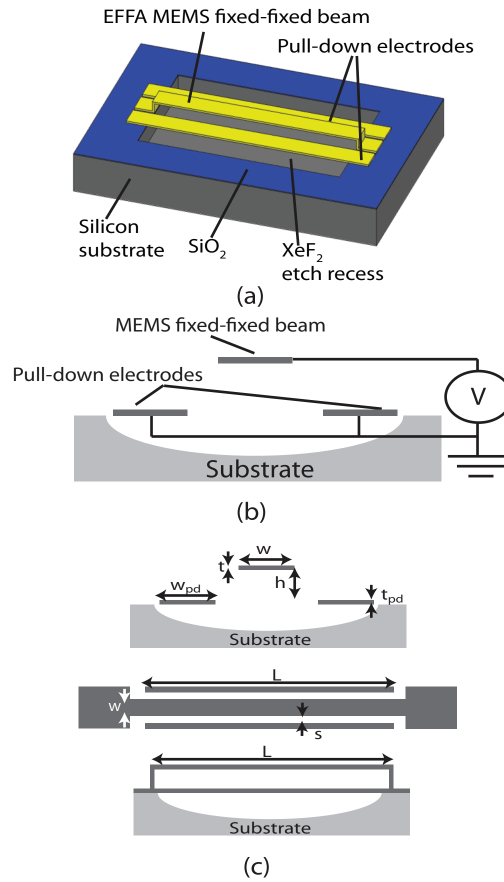

Figure 1. Schematic of proposed electrostatic fringing-field MEMS fixed-fixed beam. (a) 3D and (b) 2D perspective with biasing schematic. (c) Schematic of electrostatic fringing-field configuration with labeled beam geometrical parameters.

the gap height versus voltage characteristics of the electrostatic fringing-field actuator. Section 3 discusses geometrical design considerations for the EFFA MEMS actuators based on the newly developed design expression. Section 4 describes the dynamic behavior of the underdamped actuator and the design of the DC-dynamic input bias. Lastly, section 5 presents the experimental validation.

2. Modeling

Existing closed-form solutions (as in [9], [18], and [19]) considers a piston like motion and neglects spring softening effects along with the spring hardening effects associated with the load-deflection characteristics of a uniformly loaded fixed-fixed beam. In addition, the model becomes increasingly complex when one must consider the nature of fixed boundary conditions, nonuniformity of the electrostatic pressure due to charge redistribution, effects of residual stress, and the developed nonuniform stress distribution due to the stretching of the beam. This leads to inaccurate prediction of the voltage

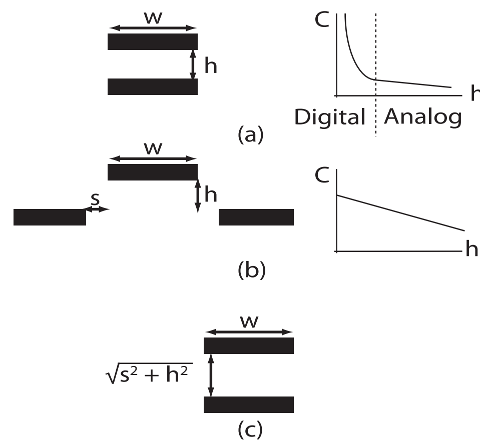

Figure 2. Qualitative derivation of proposed electrostatic model for the fringing-field capacitor. (a) Standard parallel-plate capacitor model with corresponding capacitance versus vertical gap height characteristics; (b) fringing-field capacitor model with corresponding capacitance versus vertical gap height characteristics; (c) proposed qualitative model for fringing-field capacitor.

versus gap height characteristics. Considering this plethora of issues, a hueristic model that maps the equivalent force through an extracted fitting constant to the familiar parallel-plate expression is chosen as a means by which to develop the design expression for the fringing-field actuator. Fig. 2 illustrates this phenomenological mapping approach. Both capacitor topologies, the parallel-plate field (Fig. 2a) and the fringing-field (Fig. 2b) share similar capacitance versus gap height characteristics when the parallel-plate field capacitor is in its stable region of operation. Fig. 2c is the proposed capacitor topology that maps the fringing-field topology to the familiar parallel-plate field topology.

The electrostatic fringing-field force, F_{effz}, is given by the following equation

$$F_{effz} = \frac{1}{2}V^2\frac{dC_{ff}(h)}{dh} = -\frac{1}{2}\frac{\epsilon_0 L(h_0 - h)we^m V^2}{(s^2 + (h_0 - h)^2)^{3/2}} \tag{1}$$

where V is the applied electrostatic bias, C_{ff} is the fringing-field capacitance, ϵ_0 is the permitivitty of free space, L is the length of the fixed-fixed beam, h_0 is the initial gap height when no bias is applied, while h is a gap for a given applied bias, w is the width of the fixed-fixed beam, s is the horizontal gap between the pull-down electrodes and the fixed-fixed beam, and e^m is the correction factor specifically for the electrostatic force expression. In order to facilitate at-a-glance first-principle-physics insight for rapid device design and optimization, the gap height of the heuristic model is the hypotenuse of the 90° triangle created by the sides s and h. Beam curvature will be embedded in the expression for the correction factor due to direct extraction of fitting parameters from numerical simulations of the beam deflection in response to an applied bias.

In static equilibrium F_{effz} is balanced by the mechanical restoring force, F_m, of the suspension. Equilibrium is expressed as

$$F_m = F_{effz} \tag{2}$$

$$k_z(h_0 - h) = \frac{1}{2}\frac{\epsilon_0 L(h_0 - h)we^m V^2}{(s^2 + (h_0 - h)^2)^{3/2}} \tag{3}$$

where k_z is the linear spring constant of the fixed-fixed beam in the vertical direction. The 1-D spring constant for a fixed-fixed beam with a load distributed across the entire beam is given by [1]

$$k_z = 32Ew\left(\frac{t}{L}\right)^3 + 8\sigma(1-\nu)w\left(\frac{t}{L}\right) \tag{4}$$

where E is the Young's modulus of the material, t is the thickness of the fixed-fixed beam, σ is the biaxial residual stress and ν is the Poisson's ratio of the material.

To find an expression for m we solve equation (3) for the drive voltage

$$V = \sqrt{\frac{2k_z(s^2 + (h_0 - h)^2)^{3/2}}{\epsilon_0 we^m L}} \tag{5}$$

When numerically solving for m, it is convenient to rewrite equation (5) as

$$\sqrt{\frac{2k_z(s^2 + (h_0 - h)^2)^{3/2}}{\epsilon_0 we^m L}} - V = 0 \tag{6}$$

The roots of equation (6) relate the gap height h (the dependent variable) to the drive voltage V (the independent variable). Coupled boundary element electrostatic and finite element mechanical method simulation with CoSolve in CoventorWare was used to compute h from V. Matlab was used to numerically calculate m. The obtained m values corresponding to each pair of h and V for equation (6) were plotted as a function of the normalized vertical gap height, $h/1$-μm, h_n. A logarithmic regression was used to curve fit the plot of the m values. This is given by

$$m = a_1 ln(h_n) + a_2 \tag{7}$$

where a_1 and a_2 are fitting constants based on the actuator geometrical parameters. Through further curve fitting the fitting constants have the following form

$$a_1 = a_{11} ln(s_n) + a_{12} \tag{8}$$

$$a_2 = a_{21} ln(s_n) + a_{22} \tag{9}$$

$$a_{11} = a_{111} ln(w_n) + a_{112} \tag{10}$$

where w_n and s_n are the normalized fixed-fixed beam width, $w/1$-μm, and normalized horizontal gap, $s/1$-μm, respectively. The values of the fitting coefficients are a_{11} = -0.31246 , a_{12} = -0.42129, a_{21} = 1.038679, a_{111} = -0.989331 and a_{112} = 1.053367.

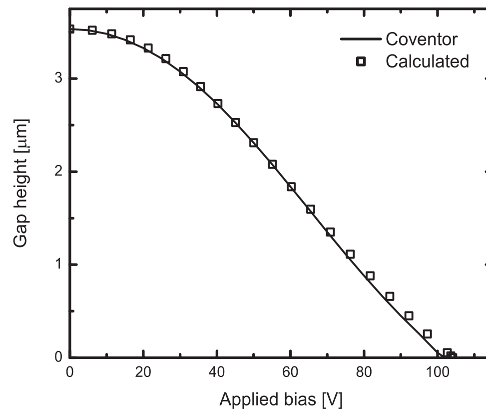

Figure 3. Comparison between the simulated and calculated voltage versus gap height characteristics. Beam dimensions $L = 400$ μm, $w = 10$ μm, $s = 5$ μm, and $t = 1$ μm.

Table 1. Simulated Dimensions and Material Parameters of Electrostatic Fringing Field Actuator

Parameter	Value
Beam length (L)	250−500 μm
Beam width (w)	10−25 μm
Beam thickness (t)	1 μm
Fringing-field pull-down electrode spacing (s)	2−8 μm
Pull-down beam width (w_{pd})	10−25 μm
Pull-down beam thickness (t_{pd})	1 μm
Vertical gap height (h)	0−4 μm
Au Young's modulus (E)	80 GPa
Au Poisson's ratio (ν)	0.44

The beam parameters for the simulated geometries are listed in Table 1. Fig. 3 illustrates a typical applied bias versus gap height response curve comparison between the simulated and calculated result. The error is 5.6 % for typical MEMS geometries. The percent error changes depend on the values of s and h. What is consistent among all simulations is that for small deflections within 1.5% of the total gap the error is $\geq$ 10 %. The largest overall errors were observed for gaps $s = 2$ μm, $s = 3$ μm and $s = 4$ μm. The reason for this being the case is that at these gaps the C−h characteristics were not as linear as our approximation asserts. The shape of the C−h curves for these s values in particular resembles a parallel-plate capacitor that is near its unstable region of operation. It was obsereved that for $s \geq 5$ μm the error was well below 10% for beam deflection greater than 1.5% of the total gap height. Secondarily, we assumed that t was infinitely thin with respect to device dimensions which was not necessarily true. When $s = 2$ μm, 3 μm and 4 μm the t/s ratio becomes 0.5, 0.3 and 0.25, respectively. Therefore the infinitely thin approximation is poor for these horizontal gaps.

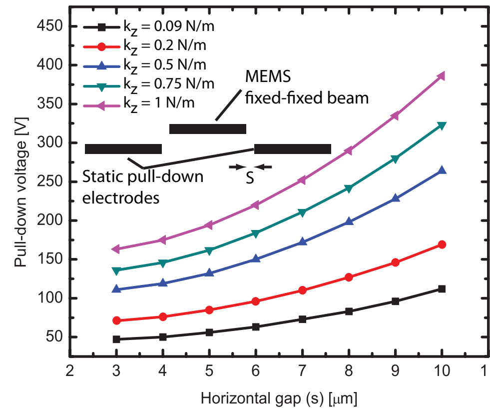

Figure 4. Applied bias needed to close the gap, pull-down voltage, versus horizontal spacing for various spring constants. The applied bias is calculated with the proposed model in this paper. The initial gap height for the calculated result is $h_0 = 4\ \mu$m.

3. Example Cases

3.1. Spring Constant and Horizontal Gap Considerations

The design of EFFA MEMS is straightforward. For a given geometry, we can rapidly compute the bias voltage needed to pull-down the beam. The most critical aspect of fringing-field MEMS that needs close attention is its spring constant. Due to the weak forces provided by the electrostatic fringing fields and lack of contact forces, low spring constant designs ≤ 1 N/m may be necessary. Fig. 4 illustrates the applied bias versus horizontal gap for several spring constants. The k_z in the plot is the total spring constant due to geometry and residual stress. It is evident from the plot that the mechanical restoring force can easily exceed the electrostatic force resulting in high applied bias. Therefore care must be taken in choosing the beam material, dimensions and in reducing biaxial residual mean stress as much as possible. In section 5.1 a fabrication technology is introduced that uses electroplated Au, a silicon sacrificial layer and a dry release to achieve < 10 MPa biaxial mean stress.

3.2. Impact of Pull-down Electrode Geometry

The thickness and width of the pull-down electrodes do not necessarily need to be the same as that of the movable membrane. The device footprint can be reduced by decreasing the width of the pull-down electrodes. From an electrostatic perspective we are concerned with maintaining the force. Fig. 5 illustrates the reduction in the computed capacitance ratio when $w_{pd} < w$. The capacitance is computed numerical with Coventor. Fig. 6 illustrates the impact of t_{pd} thickness on the capacitance ratio. Capacitance at $V = 0$ V is represented by C_U, and capacitance when the voltage pulls the beam completely down ($V = V_{down}$) is represented by C_D. Similar to the impact of the beam width on capacitance, increasing t_{pd} has a marginal effect on C_D/C_U when $t_{pd} > t$ for $s > 1\ \mu$m. On the other hand, for $s \leq 1\ \mu$m it is shown that the C_D/C_U

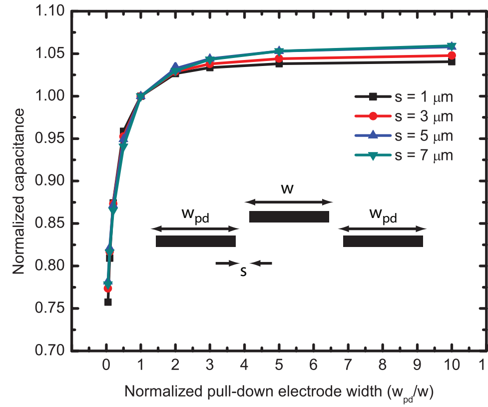

Figure 5. Simulated electrostatic fringing-field capacitance versus normalized pull-down electrode width for $h_0 = 2\ \mu$m and $t = 1\ \mu$m.

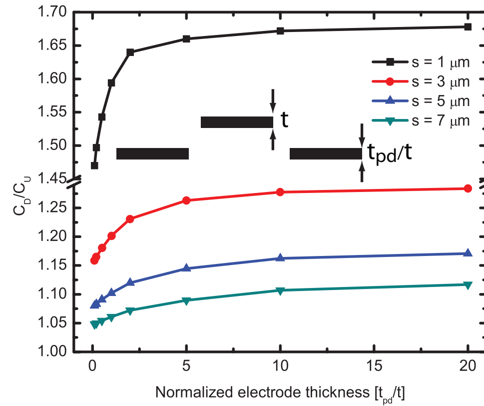

Figure 6. Simulated electrostatic force versus normalized pull-down electrode thickness.

ratio can be improved, resulting in lower applied biasing. However, achieving $s \leq 1\ \mu$m may be difficult in practice with low cost MEMS processes and therefore $s \geq 3\ \mu$m is recommended and will result in applied biases that are close to the case when $t_{pd} = t$.

Mechanically we are concerned with the pull-down electrodes remaining fixed. This is a concern due to the fabrication technology implemented in this work where the entire substrate is removed from beneath the beams (please see Fig. 10 in Section 5.2), thereby releasing the pull-down electrodes and facilitating an undesirable deflection in response to an applied bias. In order to ensure the pull-down electrodes remain fixed, the spring constant of the pull-down electrodes needs to be greater than that of the movable beam. The spring constant is proportional to t^3. For example, ignoring the residual stress term, if $w_{pd} = 3w$ and $t_{pd} = 3t$ then the pull-down electrode will have a spring constant that is approximately 10 times greater than the movable beam. Alternatively, if device footprint is not critical, then merely increasing the width of the pull-down electrodes will result in a higher spring constant.

4. Switching Time Considerations

4.1. Inertia-limited Calculation

The penalty paid for the robust EFFA device design is a substantial decrease in mechanical damping coefficient, b, and an increase in the fixed-fixed beam mechanical quality factor, Q_{ff}, which is indicative of a device with a long settling time (100s of microseconds to milliseconds). The damping coefficient is calculated by the following [1]

$$b = \frac{k_z}{2\pi f_{m0} Q_{ff}} \tag{11}$$

where f_{m0} is the mechanical resonant frequency of the MEMS membrane. The mechanical quality factor, Q_{ff}, can be approximated by the following expression [1]

$$Q_{ff} = \frac{\sqrt{E\rho}t^2}{\mu(\frac{wL}{2})^2} g_0^3 \tag{12}$$

where E is the Young's modulus of the beam material, ρ is the density of the beam material, g_0 is the gap between the fixed-fixed beam and the underlying substrate, and t is the beam thickness. The symbol μ is the coefficient of viscosity and at standard atmospheric temperature and pressure is calculated to be 1.845×10^{-5} kg/m·s. It is readily observed that b and Q_{ff} are strongly dependent on g_0. The EFFA MEMS topology in this work has the substrate completely removed from beneath the beam. As a result, g_0 is typically ≥ 20 μm. This correlates to a $b < 10^{-7}$ kg/s and a $Q_{ff} \geq 2$. Based on the low b and relatively high Q_{ff}, the fixed-fixed beam is considered an inertia-limited system (acceleration limited). Therefore, we can use the the following simplified closed-form expression to calculate the switching time for the fixed-fixed beams [1]

$$t_{down} \simeq 3.67 \frac{V_{down}}{2\pi f_{m0} V_{app}} \tag{13}$$

where V_{down} is the voltage needed to pull the beams to the desired gap height and V_{app} is the applied bias which is typically $1.2 - 1.4 V_{down}$ to result in fast switching time. The mechanical resonant frequency of the fixed-fixed beam is represented by f_{m0} and is calculated by the following expression

$$f_{m0} = \frac{1}{2\pi} \sqrt{\frac{k_z}{m_{eff}}} \tag{14}$$

where k_z represents the spring constant of the fixed-fixed beam due to a distributed load applied over the entire beam and is used from (4). We can calculate the effective mass, m_{eff}, of the fixed-fixed beam from [1]

$$m_{eff} = 0.44 \rho t w L \tag{15}$$

The m_{eff} and k_z for a fixed-fixed beam with $w = 10$ μm, $L = 400$ μm, $t = 0.45$ μm, and residual mean stress, σ, of 5 MPa are 1.5×10^{-11} kg and 0.27 N/m, respectively. The

calculated f_{m0} is 21 kHz. The calculated switching time based on (13) for the fixed-fixed beam based solely on its inertia is 28 μs.

Fig. 7 illustrates the typical dynamic step response for a fixed-fixed beam that is underdamped. This is a well-known response and has several key performance metrics which are labeled on the plot. The metrics are: final gap height, G_f, peak gap height, G_p, rise time, t_r, peak time, t_p, and settling time, t_t. Typically, t_r is defined as the time it takes to get from $0.1G_f$ to $0.9G_f$. While t_s is defined as the time it takes to get within 5 % of G_f. For very low b, the physical mechanisms that provide damping is dissipation in the beam anchors and the interface granules in the beam itself [1]. Consequently the settling time of the fixed-fixed beam > 1 ms. This relatively long settling time will be observed at every gap height since the damping surface is relatively far away from the fixed-fixed beam. This lack of squeeze film damping can be alleviated by employing DC-dynamic biasing.

4.2. Calculation Based on DC-Dynamic Biasing

The dynamic waveform proposed in this paper exploits the physics of the underdamped second-order step response in order to explicitly quantify the necessary bias voltages and timings that will improve the switching time. As illustrated in fig. 7, at G_p the velocity of the beam is at a minimum. This is the most opportune time, t_p, to apply an electrostatic bias, resulting in a fast settling time. Fig. 8 illustrates the DC-dynamic biasing concept. The red curve represents the DC-dynamic bias waveform while the black curve represents the deflection of the fixed-fixed beam in response to the applied bias. The gap heights G_2 and G_4 are the peak gap heights of G_1 and G_3, respectively. The times t_2 and t_4 are when the bias is applied to hold the beam at the G_2 and G_4 gap heights, respectively. The times t_1 and t_3 are user defined, however, $t_2 - t_1 = t_p$ and $t_4 - t_3 = t_p$. Lastly, the voltages V_1, V_2, V_3, and V_4 are the voltages needed to obtain the steady state gap heights G_1, G_2, G_3, and G_4, respectively. Both the voltages and gap heights are found with the heuristic model presented in Section 2.

In order to find G_2 and G_4, the percent overshoot, $\%OS$, must be obtained. The overshoot in an underdamped second order system can be expressed as a function of the fixed-fixed beam geometrical parameters through Q_{ff}. First, the damping ratio, ζ is expressed as

$$\zeta = \frac{b}{2m_{eff}\omega_{m0}} \tag{16}$$

We can relate ζ to Q_{ff} by the following

$$\zeta = \frac{1}{2Q_{ff}} \tag{17}$$

Now we can replace ζ by Q_{ff} for the time parameters

$$t_r = \frac{2.16(\frac{1}{2Q_{ff}}) + 0.6}{\omega_{m0}} \tag{18}$$

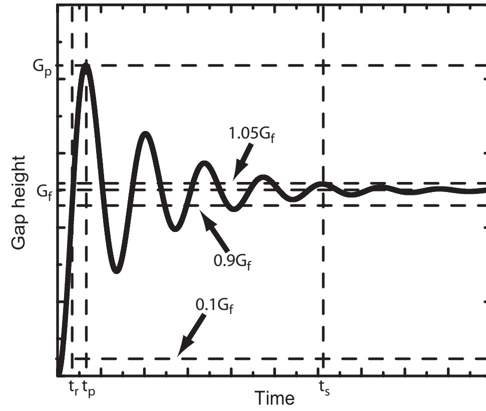

Figure 7. Sketch of typical under-damped second order system response to a unit-step input. Key metrics are noted: peak gap G_p, final gap, G_f, rise time, t_r, peak time t_p, and settling time, t_s.

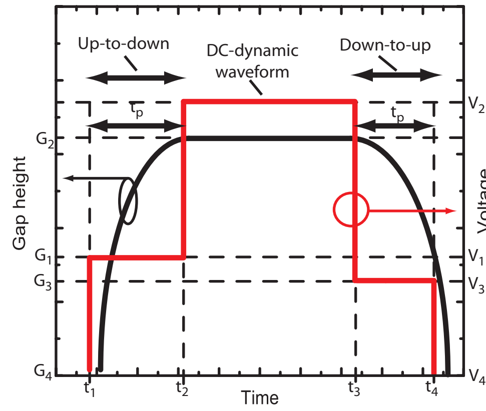

Figure 8. Sketch of typical fixed-fixed beam response to an input DC-dynamic biasing waveform.

$$t_p = \frac{\pi}{\omega_{m0}\sqrt{1-\zeta^2}} = \frac{\pi}{\omega_{m0}\sqrt{1-(\frac{1}{2Q_{ff}})^2}} \tag{19}$$

$$t_s \approx \frac{3}{\zeta\omega_{m0}} \approx \frac{6Q_{ff}}{\omega_{m0}} \tag{20}$$

The t_s in (20) is for a settling time that is within 5% of the steady state equilibrium gap height. Finally, the percent overshoot, $\%OS$, can also be expressed as a function of Q_{ff}

$$\%OS = 100 \times e^{\frac{-\zeta\pi}{\sqrt{1-\zeta^2}}} = 100 \times e^{\frac{-\frac{\pi}{2Q_{ff}}}{\sqrt{1-(\frac{1}{2Q_{ff}})^2}}} \tag{21}$$

We can obtain an approximate value for Q_{ff} based on t_s from simulation or measurements. For a fixed-fixed beam with $t_s = 2$ ms and $f_{m0} = 21$ kHz, $Q_{ff} = 44$, $b = 4.6 \times 10^{-8}$ kg/s (based on (11)), $t_p = 23.7$ μs, $t_r = 4.7$ μs, and $\%OS = 96.5$. Tables 2 and 3 shows the calculated voltage and timing parameters, respectively, for an

Table 2. Designed Voltage Parameters of DC-Dynamic Bias Waveform

State	V_1	V_2	V_3	V_4
20 V	13 V	20 V	13 V	0 V
30 V	17 V	30 V	17 V	0 V
40 V	29 V	40 V	29 V	0 V
50 V	36 V	50 V	36 V	0 V
60 V	43 V	60 V	43 V	0 V
70 V	51 V	70 V	51 V	0 V
80 V	55 V	80 V	55 V	0 V
90 V	60 V	90 V	60 V	0 V

Table 3. Designed Time Parameters of DC-Dynamic Bias Waveform

t_1	t_2	t_3	t_4
0 μs	30 μs	4 ms	4.03 ms

example DC-dynamic waveform based on Fig. 8 for a beam with $L = 400$ μm, $w = 10$ μm, $t = 0.45$ μm, and $s = 8$ μm.

5. Experimental Validation

5.1. Fabrication Technology

Fig. 9 summarizes the three-mask process for the fabrication of EFFA MEMS fixed-fixed beams. The fixed-fixed beams are fabricated on a low-resistivity silicon substrate (approximately 1−10 Ω-cm) with a thickness of 525 μm and 5000 $\AA$ of thermally grown SiO_2. The fabrication starts with patterning the SiO_2 with buffered hydrofluoric acid. This etch is used to create the mask layer for the subsequent bulk micromachining for the silicon sacrificial layer. Next, we perform a bulk etch of the silicon substrate with tetramethyl ammonium hydroxide (TMAH) 45 % by weight at 80°C with stirrer spin speed of 400 rpm. This etch is used to create the vertical gap height offset between the movable fixed-fixed beam and the static pull-down electrodes. After completing the bulk etch, the next step is to strip all of the oxide from the substrate and thermally grow another 5000 $\AA$ of SiO_2. Subsequently, we pattern the SiO_2 to expose the silicon which serves as the sacrificial layer for the final release of the fixed-fixed beams. A thin layer (1000 $\AA$) of low stress Au is sputter deposited. A very thin (<20 nm) Ti adhesion layer is used as a seed layer. Next, we create a photoresist mold that defines the geometry of the fixed-fixed beam. Then we electroplate Au to the desired thickness of the fixed-fixed beam. Electroplating is chosen over sputtering or evaporating because it allows the critical lateral design dimension to be realized (∼4 μm) as well as providing a low-stress thin film. Also, electroplating conforms to the topological difference introduced by the silicon bulk etch much better than evaporation and sputtering. After electroplating we

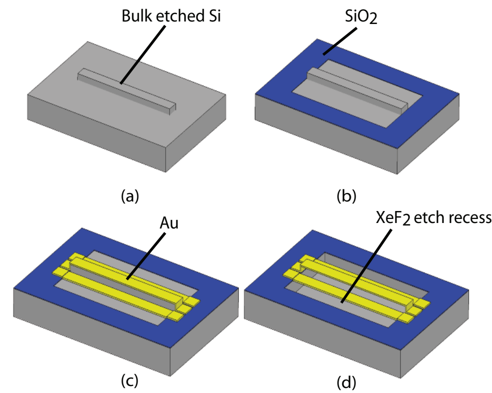

Figure 9. Process flow of the EFFA MEMS bridge. (a) TMAH bulk etch, (b) wet thermal oxidation and oxide etch to expose sacrificial silicon, (c) Au deposition and patterning of fixed-fixed beams and pull-down electrodes and (d) XeF_2 dry release of fringing-field actuators.

strip the photoresist mold using a standard dedicated photoresist stripper. The seed layer is wet etched by submerging the entire sample in a dedicated gold etchant followed by a subsequent titanium etchant. It was observed that approximately for every 100 nm of sputtered Au etched, 400 nm of electroplated Au is etched. Since the primary fixed-fixed beam metal is unprotected and will be attacked while etching the seed layer, when electroplating the fixed-fixed beam we grow the layer to be a little thicker than the design in order to compensate. Lastly, a dry isotropic XeF_2 etch that selectively attacked the silicon and released the Au fixed-fixed beams is the final step.

Two key process steps make this fabrication successful: 1) low residual stress Au film deposition and 2) the XeF_2 dry release. As explained in Section 3.1 the EFFA force is quite low. As a result, if the residual mean tensile stress is on the order of typical stresses for MEMS thin films (>60 MPa), the drive voltage will become excessively high and the reliability of EFFA MEMS may be compromised. To remedy this, we carefully characterized the electroplating recipe to produce a film with extremely low mean stress. In addition, the sacrificial layer type played an important role in ensuring low mean tensile stress [27]. This is achieved by using silicon as the sacrificial layer type. For the beams measured in this study, we extracted mean stresses of 1−8 MPa using the newly developed model. Lastly, dry release with XeF_2 enables high yield processing by making stiction due to high surface tension virtually impossible.

5.2. Gap Height Versus Applied Bias Measurement

Figs. 11 - 15 show the measured results for 5 fixed-fixed beams with different s, h_0, L and σ parameters. A Young's modulus of 35 GPa is used in the calculation for the electroplated gold [28]. The deflection versus voltage characteristics of the beams are measured with an Olympus LEXT OLS-3000 laser scanning confocal microscope [29]. The measurements have an uncertainty of ±50 nm. The model demonstrates good

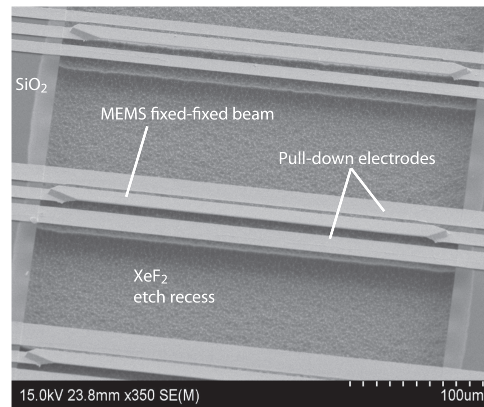

Figure 10. Scanning electron micrograph of EFFA MEMS bridges.

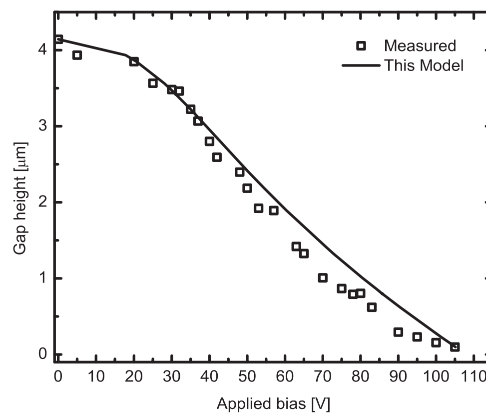

Figure 11. Measured gap height versus applied bias of EFFA fixed-fixed beams: $w = 10$ μm, $t = 0.46$ μm, $L = 350$ μm, $s = 4$ μm, and $\sigma = 4$ MPa.

agreement with the experiment. By pursuing an heuristic approach and basing the model on the exact curvature of the fixed-fixed beam, the trajectory is inherently tracked. This accounts for several electromechanical phenomena listed in the beginning of Section 2 that are difficult to capture in a compact closed-form model. The primary limiting factor in our model, like all current models, is process based.

5.3. Switching Time Measurement

The switching time measurements are captured with a polytec laser doppler vibrometer (LDV) [30] in the setup illustrated in Fig. 16. The function generator is connected to a linear high-voltage high-speed amplifier in order to achieve the necessary voltages to actuate the electrostatic fringing-field fixed-fixed beams. The applied biases and timings are found in real-time by viewing the LDV output and making manual adjustments on the function generator as the beams are actuating.

Figs. 17 and 18 illustrates the switching time of the EFFA MEMS fixed-fixed beam for a standard unit-step bias waveform and the DC-dynamic input for the 60 V gap height. Figs. 19 and 20 illustrates how the DC-dynamic bias waveform can be used

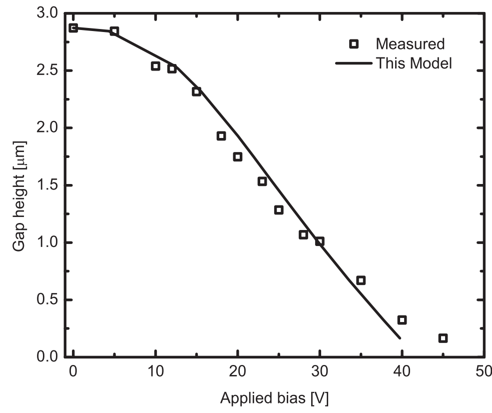

Figure 12. Measured gap height versus applied bias of EFFA fixed-fixed beams: w = 10 μm, t = 0.46 μm, L = 600 μm, s = 4 μm, and σ = 4 MPa.

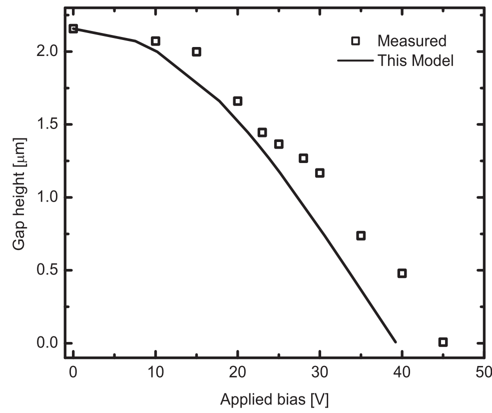

Figure 13. Measured gap height versus applied bias of EFFA fixed-fixed beams: w = 10 μm, t = 0.46 μm, L = 700 μm, s = 6 μm, and σ = 4 MPa.

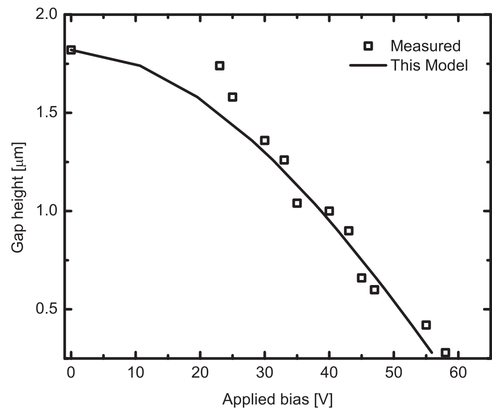

Figure 14. Measured gap height versus applied bias of EFFA fixed-fixed beams: w = 10 μm, t = 0.46 μm, L = 700 μm, s = 8 μm, and σ = 7 MPa.

for all gap heights. Table 4 and 5 shows the voltages and times, respectively, used to achieve the measured gap height positions shown in Figs. 19 and 20. By using the DC-dynamic bias waveform, the settling time reduces from $\sim$ 2 ms down to $\sim$ 35 μs for

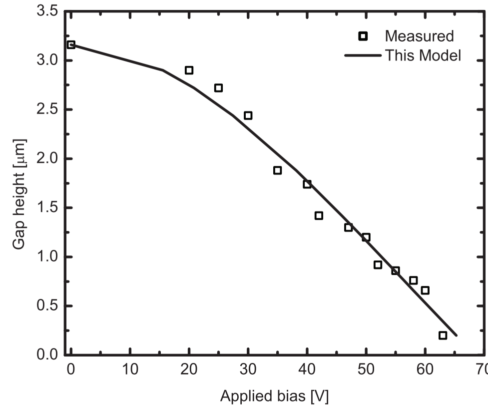

Figure 15. Measured gap height versus applied bias of EFFA fixed-fixed beams: w = 10 μm, t = 0.46 μm, L = 350 μm, s = 8 μm, and σ = 1 MPa.

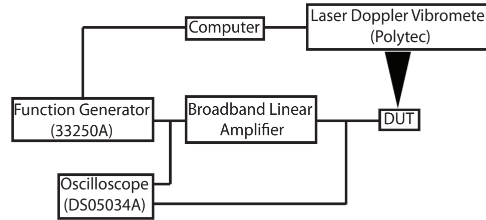

Figure 16. Measurement setup for switching time.

Table 4. Measured Voltage Parameters of DC-Dynamic Bias Waveform

State	V_1	V_2	V_3	V_4
20 V	14.2 V	20 V	13.8 V	0 V
30 V	21.2 V	30 V	20.4 V	0 V
40 V	28 V	40 V	27 V	0 V
50 V	34.6 V	50 V	33.2 V	0 V
60 V	41 V	60 V	39 V	0 V
70 V	46 V	70 V	44.4 V	0 V
80 V	52.4 V	80 V	49.4 V	0 V
90 V	57.2 V	90 V	54.6 V	0 V

both up-to-down and down-to-up states. It is observed that the calculated switching time using (13) and (19) are 28 μs and 23.7 μs, respectively, for a beam with w = 10 μm, L = 400 μm, t = 0.45 μm, s = 8 μm, and σ = 5 MPa. It is also observed from (13) and (19) that t_{down} and t_p are $\propto \sigma^{-1/2}$. Therefore small changes in the residual stress can give large changes in the switching time calculation. For example, the switching time for the same fixed-fixed beam with a residual stress of 3 MPa and 5 MPa results in a calculated switching time of 35 μs and 28 μs, respectively, using (13). Using (19), the calculated times are 30 μs and 23.7 μs, respectively. As with the compact model for calculating the applied bias, the switching time model is also limited by the processing parameters of the film.

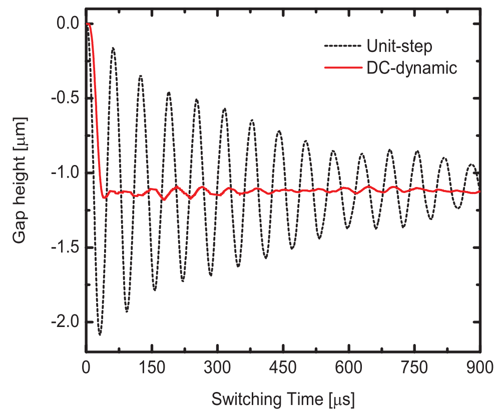

Figure 17. Measured up-to-down switching time of the 60 V gap height of the EFFA MEMS fixed-fixed beam in response to a typical unit step and DC-dynamic applied bias.

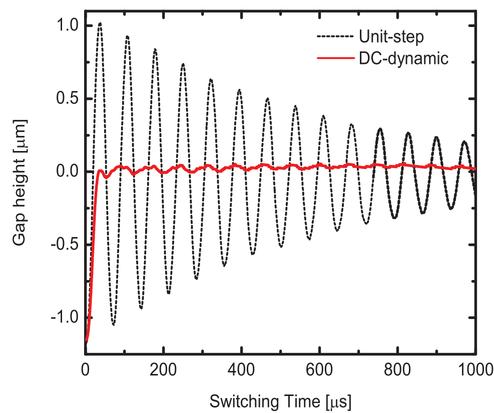

Figure 18. Measured down-to-up switching time from the 60 V gap height of the EFFA MEMS fixed-fixed beam in response to both a typical unit step and DC-dynamic applied bias.

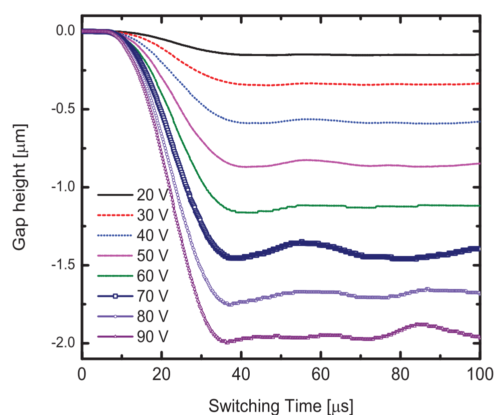

Figure 19. Measured up-to-down switching time of the EFFA MEMS fixed-fixed beam in response to both a DC-dynamic applied bias for several intermediate gap heights.

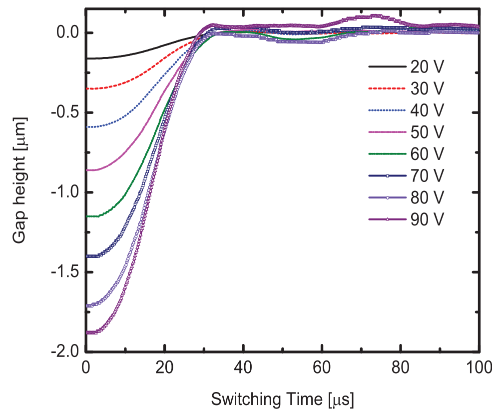

Figure 20. Measured down-to-up switching time of the EFFA MEMS fixed-fixed beam in response to a DC-dynamic applied bias for several intermediate gap heights.

Table 5. Measured Time Parameters of DC-Dynamic Bias Waveform

State	t_1	t_2	t_3	t_4
20 V	5 μs	41 μs	4 ms	4.036 ms
30 V	5 μs	41 μs	4 ms	4.036 ms
40 V	5 μs	41 μs	4 ms	4.036 ms
50 V	5 μs	40 μs	4 ms	4.035 ms
60 V	5 μs	42 μs	4 ms	4.035 ms
70 V	5 μs	39 μs	4 ms	4.034 ms
80 V	5 μs	37 μs	4 ms	4.033 ms
90 V	5 μs	36 μs	4 ms	4.032 ms

6. Discussion

The method presented in this work demonstrates significant improvement in switching time for electrostatic fringing field actuators where the substrate is removed. This topology is chosen because it demonstrates a worst case scenario where squeeze film damping is effectively zero. However, many designs of electrostatic MEMS actuators and sensors leave the underlying substrate intact. The method presented in this work is independent of whether a substrate is beneath the device or not. As long as the device is underdamped and its gap height versus voltage characteristics can be calculated, the presented method will be useful in improving switching time.

7. Conclusion

The design, fabrication, and experimental validation of fast switching in severely underdamped electrostatic fringing-field actuators is presented. An $> 50\times$ switching time improvement is achieved through the use of DC-dynamic biasing. Electrostatic fringing-field actuation is used due to its robust device design and inherently low damping conditions. A qualitative model that maps the fringing-field capacitance

of the EFFA MEMS actuator as a parallel-plate capacitor in its analog capacitance versus gap regime is presented and discussed. A quantitative compact model for the voltage versus gap height characteristics based on the effective parallel-plate model is successfully developed and validated with numerical simulation. The error between the model and the numerical simulation results is less than 5.55% for typical MEMS geometries. Electromechanical design considerations is presented based on the proposed compact model and numerical simulation. A DC-dynamic waveform is designed based on the newly derived model. Experimental validation of the model is performed and for a given voltage good agreement is demonstrated with typically less than 10% error. With dynamic biasing the measured up-to-down and down-to-up switching time of the actuator is $\sim 35\ \mu$s. On the other hand, conventional step biasing results in a switching time of ~ 2 ms for up-to-down and down-to-up states. Future work includes finding a common waveform for multiple switches in a system.

8. Acknowledgment

The authors wish to thank Ryan Tung for his assistance and useful technical discussions. The authors also wish to acknowledge the assistance and support of the Birck Nanotechnology Center technical staff. This work was supported by the Defense Advanced Research Projects Agency under the Purdue Microwave Reconfigurable Evanescent-Mode Cavity Filters Study. And also by NNSA Center of Prediction of Reliability, Integrity and Survivability of Microsystems and Department of Energy under Award Number DE-FC5208NA28617. The views, opinions, and/or findings contained in this paper/presentation are those of the authors/presenters and should not be interpreted as representing the official views or policies, either expressed or implied, of the Defense Advanced Research Projects Agency or the Department of Defense.

References

[1] Rebeiz G 2003 *RF MEMS: Theory, Design and Technology* (John Wiley and Sons)
[2] Senturia S D 2001 *Microsystem Design* (Springer)
[3] Bouchaud J 2011 *Propelled by HP Inkjet Sales, STMicroelectronics Remains Top MEMS Foundry* http://www.isuppli.com/MEMS-and-Sensors/News/Pages/Propelled-by-HP-Inkjet-Sales-STMicroelectronics-Remains-Top-MEMS-Foundry.aspx
[4] Lantowski K G D 2011 *The Future of Cinema Has Arrived: More Than 50,000 Theatre Screens Worldwide Feature The Brightest, 2D/3D Digital Cinema Experience With DLP Cinema®* http://www.dlp.com/technology/dlp-press-releases/press-release.aspx?id=1510
[5] Bosch-Wachtel T 2011 *Knowles Ships 2 Billionth SiSonic™ MEMS Microphone* http://pressrelease.smartoman.com/?p=2810
[6] Burke J 2012 *mirasol Display Capabilities Add Color and Interactivity to Improve User Experience for Renowned Jin Yong Branded Device* http://www.mirasoldisplays.com/press-center/press-releases/2012/01/koobe-taiwan%E2%80%99s-leading-e-reader-manufacturer-and-qualcomm-bring
[7] Bettler D 2011 *MEMStronics Captures Prestigious R & D 100 Award* http://www.memtronics.com/files/MEMtronics_Press_Release7_1_2011.pdf

[8] Marsh C 2008 *Omron Releases New RF MEMS Switch with Superior High Frequency Characteristics rated to 100 Million Operations* http://www.components.omron.com/components/web/pdflib.nsf/0/D69D5B6BCBE68DC2862574FD005B5141/$file/Omron_2MES-1_PR_final.pdf

[9] Rosa M A, Bruyker D D, Völkel A R, Peeters E and Dunec J 2004 A novel external electrode configuration for the electrostatic actuation of MEMS based devices *J. Micromech. Microeng.* **14** 446-51

[10] Rottenberg X, Brebels S, Ekkels P, Czarnecki P, Nolmans P, Mertens R P, Nauwelaers B, Pures R, De Wolf I, De Raedt W and Tilmans H A C 2007 Electrostatic fringing-field actuator (EFFA): application towards a low-complexity thin film RF-MEMS technology *J. Micromech. Microeng.* **17** S204-S210

[11] Allen W N, Small J, Liu X and Peroulis D 2009 Bandwidth-optimal single shunt-capacitor matching networks for parallel RC loads of Q $\gg$ 1 *Asia-Pacific Microw. Conf. (Singapore)* 2128-31

[12] Small J, Liu X, Garg A and Peroulis D 2009 Electrostatically tunable analog single crystal silicon fringing-field MEMS varactors *Asia-Pacific Microw. Conf. (Singapore)* 575-8

[13] Liu X, Small J, Berdy D, Katehi L P B, Chappell W J and Peroulis D 2011 Impact of mechanical vibration on the performance of RF MEMS evanescent-mode tunable resonators *IEEE Microw. Wireless Compon. Lett.* **21** 406-8

[14] Small J, Irshad W, Fruehling A, Garg A, Liu X and Peroulis D 2012 Electrostatic fringing-field actuation for pull-in free RF-MEMS analog tunable resonators *J. Micromech. Microeng.* **22** 095004

[15] Su J 2008 *A lateral-drive method to address pull-in failure in MEMS* (Ph.D. Dissertation Dept. Elect. Comput. Eng., University of Notre Dame)

[16] Scott S and Peroulis D 2009 A capacitively-loaded MEMS slot element for wireless temperature sensing of up to 300°C *IEEE MTT-S Int. Microwave Symp. Dig. (Boston, MA, USA)* 1161-4

[17] Scott S, Sadeghi F and Peroulis D 2009 Inherently-robust 300C MEMS sensor for wireless health monitoring of ball and rolling element bearings *IEEE Sensors (Christchurch, New Zealand)* 975-8

[18] Lee K B 2007 Non-contact electrostatic microactuator using slit structures: theory and a preliminary test *J. Micromech. Microeng.* **17** 2186-96

[19] Su J, Yang H, Fay P, Porod W and Berstein G H 2010 A surface micromachined offset-drive method to extend the electrostatic travel range *J. Micromech. Microeng.* **20** 015004

[20] Borovic B, Liu A Q, Popa D, Cai H and Lewis F L 2005 Open-loop versus closed-loop control of MEMS devices: Choices and issues *J. Micromech. Microeng.* **15** 1917-24.

[21] Pons-Nin J, Rodriquez A and Castaner L M 2002 Voltage and pull-in time in current drive of electrostatic actuators *J. Microelectromech. Syst.* **11** 196-205

[22] Czaplewski D A, Dyck C W, Sumali H, Massad J E, Kuppers J D, Reines I, Cowan W D, and Tigges C P 2006 A Soft Landing Waveform for Actuation of a Single-Pole Single-Throw Ohmic RF MEMS Switch *J. Microelectromech. Syst.* **15** 1586-94

[23] Elata D and Bamberger H 2006 On the dynamic pull-in of electrostatic actuators with multiple degrees of freedom and multiple voltage sources *J. Microelectromech. Syst.* **15** 131-40

[24] Chen K -S and Ou K -S 2009 Fast positioning and impact minimizing of MEMS devices by suppression motion-induced vibration by command shaping method *Proc. IEEE 22nd Int. Conf. Micro Electro Mech. Syst. (Sorrento, Italy)* 1103-6

[25] Chen K -S, Yang T -S and Yin J -F 2006 Residual vibration suppression for duffing nonlinear systems with electromagnetical actuation using nonlinear command shaping techniques *ASME J. Vibration and Acoustics* **128** 778-789

[26] Irvine T 1999 *Application of the Newton-Raphson Method to Vibration Problems* (Vibrationdata Publications)

[27] Garg A, Small J, Mahapatro A, Liu X and Peroulis D 2009 Impact of sacrificial layer type on thin film metal residual stress *IEEE Sensors (Christchurch, New Zealand)* 1052-5

[28] Baek C -W, Kim Y -K, Ahn Y and Kim Y -H 2005 Measurement of the mechanical properties of

electroplated gold thin films using micromachined beam structures *Sensors and Actuators A* **117** 17-27

[29] Confocal Scanning Laser Microscope LEXT OLS3100/OLS3000 User Manual 6th ed 2008 (Olympus America Inc., Center Valley, PA)

[30] Polytec Technical Manual 2010 (Polytec Inc., Irvine, CA)

[31] Maxwell Online Help 2009 (Ansys Inc., Canonsburg, PA)

[32] Design Flow in Intellisuite v8.6 2010 (IntelliSense Corp, Woburn, MA)

[33] Leus V and Elata D 2004 *Fringing Field Effect in Electrostatic Actuators* (Technion Tech. Rep. http://meeng.technion.ac.il/)

[34] Van de Meijs N and Fokkema J T 1984 VLSI circuit reconstruction from mask topology *Integration* **2** 85-119

[35] CoventorWare 2008 Analyzer Reference version 2008.010 2008 (Coventor Inc., Cary, NC)

[36] Pamidighantam S, Puers R, Baert K and Tilmans H A C, Pull-in voltage analysis of electrostatically actuated beam structures with fixed-fixed and fixed-free end conditions 2002 *J. Micromech. Microeng.* **12** 458-64